Ambient Large-Scale Template-Mediated Synthesis of High-Aspect Ratio Single-Crystalline, Chemically Doped Rare-Earth Phosphate Nanowires for Bioimaging

Fen Zhang[†] and Stanislaus S. Wong[†,‡,*]

[†]Department of Chemistry, State University of New York at Stony Brook, Stony Brook, New York 11794-3400 and [‡]Condensed Matter Physics and Materials Sciences Department, Brookhaven National Laboratory, Building 480, Upton, New York 11973

ABSTRACT A simple and effective template-mediated protocol has been developed for the large-scale, room-temperature preparation of high-aspect-ratio, single-crystalline Tb-doped $CePO_4$ nanowires, measuring ~12 nm in diameter and over 10 μm in length. Moreover, we also isolated sheaf-like bundles of nanostructures. The synthesis mechanism likely involved a crystal splitting step. The resulting nanowires demonstrated an intense redox-sensitive green photoluminescence, which was exploited, in addition to their inherently high biocompatibility and low toxicity, for potential applications in biological imaging and labeling of cells.

KEYWORDS: nanowire · metal oxide · photoluminescence · biocompatibility · cell labeling · template synthesis · crystal splitting · one-dimensional.

Manipulable nanoscale luminescent materials, many of which are either fluorescent, magnetic, or both, are increasingly being used for a number of significant biological applications including drug and gene delivery, biosensing, and bioimaging.[1] For instance, zero-dimensional (0D) nanoparticles, including quantum dots (QDs), such as CdS, CdSe, and CdTe, have been demonstrated to be highly effective for cellular and animal imaging,[2−4] since, as compared with conventional organic fluorophores (such as rhodamine and FITC), QDs exhibit high photostability, possess size-dependent emissions, and maintain high quantum yields, as well as evince broad excitation spectra and narrow emission bands. Nevertheless, the widespread use of QDs is limited by issues associated with their low light-penetration depth, potential toxicity, surface ligand incompatibility, optical blinking, and the presence of strong background fluorescence in certain analyzed systems.

As a complementary but relevant optical imaging probe, lanthanide-doped inorganic nanoparticles maintain a fluorescence, characterized by high photochemical stability, and long luminescence lifetimes (up to several microseconds).[5] In addition, as compared with conventional dyes, rare-earth lanthanide phosphate nanocrystals maintain comparatively higher quantum yields (up to 61%), lower photobleaching potential, expected low toxicity, and high chemical stability, all of which are excellent attributes for biological labeling applications. Moreover, these lanthanide probes also possess additional distinctive features, such as sharp emission bands, as determined by the nature of the lanthanide ions themselves. Furthermore, they maintain large Stokes shifts (as much as several hundred nm), such that the donor/acceptor emission signal can be detected far from the excitation wavelength with zero absorption, thereby improving overall sensitivity.[6−8]

However, to the best of our knowledge, the application of rare-earth ion-doped lanthanide phosphate nanostructures as biological labels for *in vitro* bioimaging purposes has not as yet been demonstrated. Obvious reasons for doing so would be to enhance surface-to-volume ratios as well as to influence the electric/magnetic dipole fields in these one-dimensional (1D) systems, as a result of their intrinsic shape anisotropy.

There are a number of additional advantages of creating these rare-earth-ion-doped nanomaterials as compared with their nondoped analogues. First, Tb-doped $CePO_4$ systems are capable of a luminescent

*Address correspondence to sswong@notes.cc.sunysb.edu, sswong@bnl.gov.

Received for review August 22, 2009 and accepted December 14, 2009.

Published online December 30, 2009.
10.1021/nn901057y

molecular switching behavior based on the reversible redox reaction of a Ce^{3+}/Ce^{4+} couple, rendering them sensitive to the localized redox environment within a biological context.[9,10] Second, regarding $EuPO_4$, doping can mitigate the possibility of concentration quenching in which an excess of Eu, for instance, can increase the probability of nonradiative energy migration between Eu^{3+} ions up to quenching centers where the excitation energy is lost nonradiatively.[11−13] Third, with respect to $TbPO_4$, cerium doping can more specifically improve upon the inherently weak and narrow Tb^{3+} absorption by sensitization, thereby leading potentially to higher quantum yields.[14] Therefore, herein, we have systematically investigated, for the first time, the (a) production and (b) subsequent utilization of Tb-doped $CePO_4$ ultrathin nanowires as fluorescent labels in bioimaging.

In general, the rational synthesis of inorganic 1D nanotubes and nanowires with controlled size, shape, composition, and morphology has attracted intensive research interest, as they are potential building blocks for advanced materials as well as for functional devices with applicability in areas as diverse as electronics, optics, and catalysis.[15] Specifically, lanthanide phosphate ($LnPO_4$) nanorods, measuring 20−70 nm in length with aspect ratios from 2 to 7, have been synthesized by calcination of a sol−gel at 400 °C.[16] Electrospinning has been used in conjunction with the sol−gel process as well to yield polycrystalline nanowires ranging from 60 to 300 nm, after calcination at 650−750 °C.[17,18] Generally, the hydrothermal methodology has been primarily used for the synthesis of 1D $LnPO_4$ nanostructures, measuring typically 20−60 nm in diameter with lengths from several hundred nm to several micrometers. The treatment usually involves reaction in a Teflon-lined stainless-steel autoclave often under anomalous pH conditions, at a relatively high temperature (in the range of 150−240 °C), and involving reaction times ranging from a few hours up to several days, depending on the experimental circumstances.[10,19−28] The synthesis of well-defined crystalline $CePO_4$ nanowires with a diameter of 3.7 nm was reported by use of a microemulsion reaction medium, but could take as long as a month to produce,[29] while ultrasound irradiation of an inorganic salt aqueous solution has been reported for the synthesis of $CePO_4$:Tb and $CePO_4$:Tb/$LaPO_4$ core/shell nanorods.[30] Hence, one of the key motivators of our work was to develop a more facile, milder, less technically demanding, but more cost-effective approach toward the generation of 1D $LnPO_4$ nanostructures.

Templated syntheses represent a conceptually straightforward approach to the generalized synthesis of 1D nanostructures. In this method, the template simply serves as a structural framework either around or within which another totally distinctive material can be generated *in situ* and shaped into a nanostructure with its morphology dictated by the confinement of the template scaffold. Nevertheless, templating does suffer from several drawbacks. For instance, most nanostructures previously produced by conventional templating procedures are polycrystalline,[31] in spite of the variety of different deposition strategies used, including electrochemical deposition, electroless deposition, polymerization, sol−gel deposition, and layer-by-layer deposition in nanoporous templates. The reason for the observed polycrystallinity is that many of these prior methodologies require additional postannealing steps at high temperature (*e.g.*, several hundred °C).[32−35] Moreover, the template method almost invariably suffers from the problem of relatively low product yields.[31]

Our group has recently developed a modified template technique, enabling us to prepare crystalline 1D nanostructures of a number of classes of diverse materials.[36−42] Our U-tube protocol occurs under ambient conditions; minimizes the use of either pyrophoric, flammable, or unstable precursors; and attempts to run reactions in as few steps as possible in aqueous solvents with little if any byproducts (*e.g.*, processes with an absence of volatile and toxic byproducts).

Herein, we report the first demonstration of a facile, room-temperature template-directed synthetic route toward the production of two distinctive morphologies: (a) high-purity, high-aspect-ratio, single-crystalline ultrathin nanowires (external to the template), as well as (b) sheaf-like nanowire bundles (within the template pores) of Tb-doped $CePO_4$ at room temperature. Importantly, we can easily fabricate ultrathin nanowires on a reasonably large scale, that is, >500 mg per lab run, which has previously been difficult to achieve using a template-mediated synthesis. Moreover, we have also successfully demonstrated the use of these as-prepared Tb-doped $CePO_4$ ultrathin nanowires as fluorescent labels for *in vitro* bioimaging and, furthermore, provided a series of data as to their relative nontoxicity.

RESULTS AND DISCUSSION

X-ray Diffraction. The purity and crystallinity of as-prepared Tb-doped $CePO_4$ nanowires were initially characterized using XRD (Figure 1). All of the diffraction peaks observed from the sample (top, black curve) can be readily indexed to a pure hexagonal phase formulation [space group: $P6_222$] of pristine $CePO_4$ (bottom, red curve), possessing lattice constants of a = 7.103 Å and c = 6.481 Å, which are comparable with reported database values of a = 7.055 Å and c = 6.439 Å for bulk $CePO_4$ (JCPDS File No. 34-1380). Moreover, the intensity of the (200) peak is much stronger than that of the other peaks and is distinctly different from that of bulk hexagonal $CePO_4$. Nonetheless, our data indicate that the as-obtained nanowires should grow preferentially along the [001] direction (the *c*-axis), an assertion which is further demonstrated below by HR-TEM and SAED analysis.

Electron Microscopy. ***Insights into Nanowire Formation.*** The size and morphology of our as-prepared Tb-doped Ce-

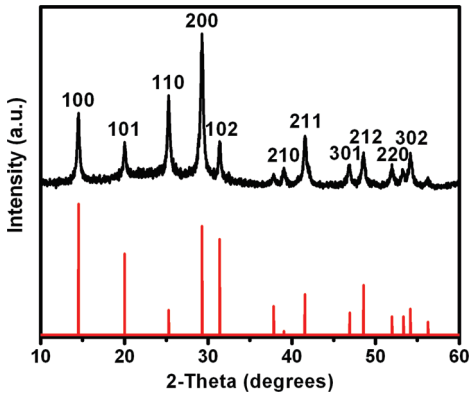

Figure 1. XRD patterns obtained from as-prepared Tb-doped $CePO_4$ nanowires (top, black) and corresponding JCPDS No. 34-1380 database standard for bulk $CePO_4$ (bottom, red).

PO_4 nanowires, collected from the U-tube solution outside the actual templates themselves, were investigated using both FE-SEM and TEM. Typical SEM and TEM images are shown in Figure 2A,B. A very large number of nanowires could be isolated, no matter what pore size dimension (e.g., 50, 100, or 200 nm) of polycarbonate membranes was used in our synthesis. In fact, for a typical reaction time of 2 h, we were able to collect as much as 600 mg per experimental run, corresponding to a reasonable 60 to 65% yield. The large quantities of nanowires synthesized are atypical of conventional template syntheses but were fully representative of the results associated with our modified protocol for this phosphate system.

On the basis of the measurements of several tens of nanowires pertaining to each of our samples, our as-prepared nanowires measured 14 $\pm$ 5 nm in diameter with a length of up to 10 $\pm$ 2 μm. Curiously, these lengths were much longer than the reported thickness of the porous template membranes (*e.g.*, 6 μm), and measured diameters were much thinner than the smallest pore diameters normally used (*e.g.*, 50 nm). In additional experiments, when we performed a number of syntheses using membranes with pore sizes measuring as small as 15 nm, the resulting nanowires (Supporting Information, Figure S1) possessed diameters ranging from 8 to 12 nm with lengths of 7 to 11 μm, consistent with our other results. Though these ultrathin nanowires tended to aggregate and cluster fairly easily, as can be observed from the SEM image (Figure 2A), sonication could readily resolve this problem, resulting in the isolation of individual nanostructures, as shown in the corresponding TEM image (Figure 2B).

The HRTEM image (Figure 2D) of a randomly chosen individual Tb-doped $CePO_4$ nanowire (Figure 2C) clearly shows resolvable planes corresponding to the [001] and [100] directions (Figure 2D). The (001) planes are oriented parallel to the nanowires' growth axis, suggesting that the growth direction of the single-crystalline nanowire occurs preferentially along the [001] direction (the *c*-axis). By contrast, the SAED pattern (Figure 2E) taken from single nanowires can be indexed to the (100) and (001) planes of a hexagonal $CePO_4$ single crystal phase, respectively. These findings are consistent with previous XRD analyses. EDS analysis (Figure 2F) confirms that the chemical signatures associated with the nanowires are composed of Tb, Ce, P, and O elements, while the Cu signal originates from the TEM grid.

The interesting nuances of our current template experiments herein are associated with two factors in particular. First, we were able to synthesize significantly thinner and shorter nanowires in the U-tubes (but not from the membrane pores themselves) than otherwise might have been expected based upon the pore diameter and membrane thickness from whence these nanomaterials were derived. Second, we could easily generate hundreds of mg of product in a given experiment as opposed to merely synthesizing a few tens of mg at a given time, as was typical of much of our previous work.[36−42] We would have expected that the morphology of our Tb-doped $CePO_4$ nanorods should have faithfully mapped out the interior spatial profile, dimensionality, and localized contours of the internal pore channels of the polycarbonate membrane scaffolds from whence these 1D structures were produced. This simplistic mechanism did not obviously play out in the current study.

Nonetheless, the observed nanorod formation is not surprising considering the crystal structure of hexagonal $CePO_4$, shown in Supporting Information Figure S2. From a structural point of view, hexagonal $CePO_4$ consists of infinite linear chains of alternating cerous and phosphate ions, extending along the *c*-axis. From a thermodynamic perspective, the bonding between these chains is considerably weaker than that within the chains, such that the activation energy for the *c*-axis direction of growth of hexagonal $CePO_4$ is lower than that for a growth direction perpendicular to the *c*-axis itself.[43] Hence, these data imply a higher growth rate along the *c*-axis, suggesting that the nanorods end up growing preferentially and anisotropically along the [001] direction, consistent with what we have observed and with what others have also noted.[10,23,26,44] Thus, the intrinsic crystal structure of $CePO_4$ itself is inherently responsible for the observed 1D growth. Indeed, our results are consistent with the model put forward by Peng *et al.*[45,46] in which one-dimensional growth only occurs if the chemical potential of monomers in solution is much higher than the highest attainable chemical potential of atoms on the surface of the nanocrystals. One other key point to note is that our synthesis is pH-dependent, which can help to define the local chemical potential.[19] The pH parameter[26] can sensitively influence the solute concentrations of both cerous and phosphate ions. As with previous reports,[27,47] we have found that a hexagonal-phase $CePO_4$ nanorod morphology was obtained when the pH value was

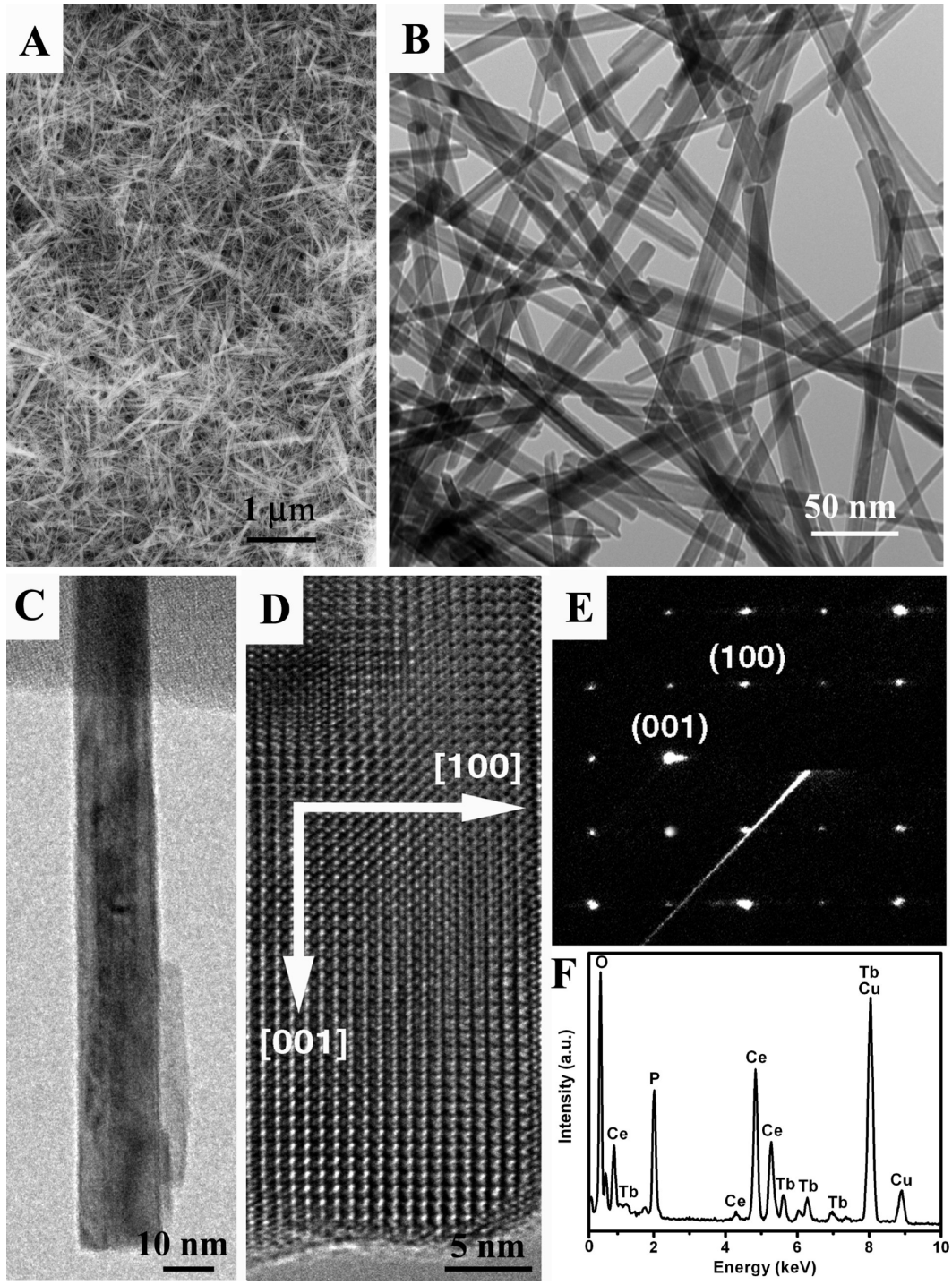

Figure 2. (A, B) Typical SEM and TEM images of as-prepared Tb-doped $CePO_4$ nanowires collected from aqueous solution; (C) TEM image of a representative single nanowire, randomly isolated from the sample; (D) HRTEM image of a representative portion of an individual nanowire; (E) corresponding SAED pattern of these nanowires; (F) EDS spectrum of Tb-doped $CePO_4$ nanowires. The Cu peaks originate from the TEM grid.

acidic, presumably aided by enhanced dissolution of cerous and phosphate ions under these conditions, thereby allowing the ions sufficient time and opportunity to adopt correct positions within the developing crystal lattices.

Insights into Sheaf-like Bundle Formation. To complicate matters, we also were able to synthesize sheaf-like bundles of Tb-doped $CePO_4$ nanostructures to the tune of ~50 mg per run, corresponding to a ~5% yield, upon removal of the template membrane itself. Figure 3 panels A and B are representative SEM and TEM images of these atypical morphologies. Specifically, each sheaf-like bundle measures ~100 nm in width, comparable to the pore diameter (nominally reported to be 100 nm

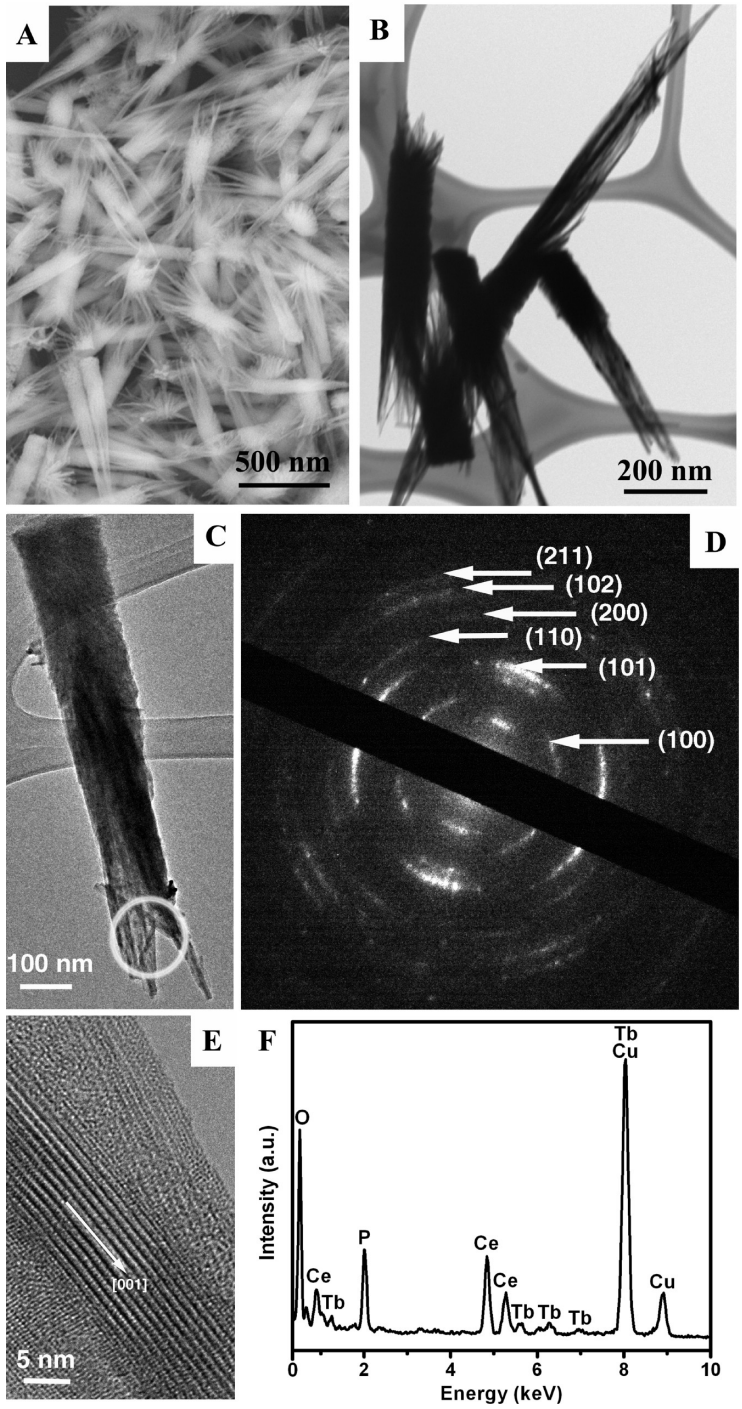

Figure 3. (A, B) Typical SEM and TEM images of sheaf-like bundles of as-prepared Tb-doped $CePO_4$ nanostructures grown the 100 nm pore channels of polycarbonate membranes; (C, D) TEM image and corresponding SAED pattern of a single half of a sheaf-like nanostructure bundle; (E) HRTEM image of a representative section at the tip of a sheaf-like bundle, highlighted by a white circle in panel C; (F) EDS spectrum of as-prepared Tb-doped $CePO_4$ sheaf-like nanostructures. The Cu peaks originate from the TEM grid.

in this case) of the commercial polycarbonate membrane. Individual constituent bristles of each bundle possess an average diameter of ~12 nm, comparable in dimension with that of the thin nanowires collected in the solution.

Although symmetric haystack-like aggregates, composed of sheaf-like bundles projecting out at *both* ends, were often obtained, asymmetric, truncated structures consisting of sheaf-like bundles protruding from only *one* end formed the majority of as-prepared products isolated from within the template membrane pores. For example, Figure 3C shows a representative, asymmetric, truncated sheaf-like bundle. The associated SAED pattern is consistent with that of pure $CePO_4$ crystals pertaining to a hexagonal structure, as indexed in Figure 3D. The slightly diffuse, textured ring pattern is con-

sistent with a sheaf-like bundle of nanoscale bristles partially aligned along the common axis. HRTEM analysis (Figure 3E) of the end of an individual sheaf-like bundle nanostructure indicates that each constituent bristle is single-crystalline without any visible defects and dislocations, although their total absence in the sample cannot be ruled out. The calculated interplanar distance is about 0.63 nm, corresponding to the (100) crystal plane of hexagonal $CePO_4$ crystals. This observation suggests that the nanoscale bristles are structurally uniform single crystals with a preferential growth direction of [001], for instance, identical to the *c*-axis of the ultrathin nanowires isolated from solution. The chemical signatures obtained from EDS spectra (Figure 3F) are identical within experimental accuracy, and only Tb, Ce, P, and O elements were observed, as expected. The Cu signal arose from the TEM grid.

The coexistence of various novel morphological motifs (including but not limited to flowers, particles, combs, and pentapods), whose individual synthesis is intimately dependent upon precise experimental conditions, has been commonly observed for a number of metal oxide systems.[48−51] In general, sheaf-like networks of nanostructures have been previously noted for β-FeO(OH),[52] iron phosphides,[53] Bi_2S_3,[54,55] lead selenides,[56] lanthanum orthovanadates,[57] CeO_2,[58] $BaWO_4$,[59] as well as Sb_2S_3 and Sb_2Se_3.[60,61] Moreover, the formation of ordered, oriented nanowire-based assemblies with bundle-like structures in the absence of copolymers and surfactants has also been observed for Eu^{3+}-doped $TbPO_4$ nanowires.[11] The exact growth mechanism associated with all of these nanomaterial motifs remains unclear. Though it has been proposed that these assemblies arise from the presence of intrinsic electric fields,[62−64] which direct the growth of dipole crystals, we believe that the splitting growth mechanism may more appropriately account for our observations.

In particular, crystal splitting is associated with fast crystal growth and depends strongly on the oversaturation of the solution.[56] It has been suggested that splitting is only possible if the oversaturation exceeds a certain critical level, unique to each material.[54] Factors known to cause crystal splitting include mechanical splitting (*i.e.*, when extra molecules appear in some layers of its crystallographic network) and chemical splitting (*i.e.*, when certain ions are present in the parent solution). Because faster growth is also expected to result in a higher density of defects in the resulting structures, the observation of crystal splitting in bundles of Bi_2S_3 nanorods led one group[44] to postulate that the strain field caused by the presence of these linear and planar defects as well as atomic distortions, created during the growth process, is a key contributor to this phenomenon.

According to a plausible crystal splitting scenario, new surface area is created each time the crystal splits and the balance between bulk and surface energies determines the particular crystal size obtainable. Therefore, under the ambient, low-temperature conditions herein, there is an initial formation of only a few nuclei just after supersaturation followed by subsequent fast growth to a state of metastability wherein crystals can grow beyond this size. It is then thermodynamically favorable for the large crystal to split, partly because of the strong adhesion of an additive, such as the H^+ highly prevalent in an acidic environment, to the newly created surface.[54] Hence, by this mechanism, a single nanowire can essentially branch into a sheaf.[53]

In many ways, this process is akin to biomineralization, which defines the nature of the modified template growth process developed in our laboratory. In the current study, the growth mechanism involves a double-diffusion crystallization process, set in a U-tube (Supporting Information, Figure S3) which enables the continuous flow of precursor ions into spatially confined membrane pores.[65−67] In a typical synthesis, one of the two half cells was filled with a 0.01 M NaH_2PO_4 solution, and the other half cell contained a solution prepared by mixing 0.05 M $CeCl_3$ solution together with $Tb(NO_3)_3$ up to a final molar concentration of 10.0%, so as to generate desired Tb-doped $CePO_4$ nanostructures. To prevent overly rapid mixing, the solutions are separated by a polycarbonate membrane that slows down diffusion and the rate of crystallization. However, when the two solutions do meet, precipitation occurs, depleting the availability of ions in the local environment of the growing crystal within the template. The nucleation rate is primarily dictated by the supersaturation of the solution. Further growth of the nanostructures is limited by diffusion of ions in this localized region.

We believe that, herein,[60,68] the initially formed ultrathin nanowires had a strong tendency to aggregate as larger ones and that the acidic medium was conducive to the self-assembly and subsequent crystal splitting of these as-formed bundles into sheaf-like patterns that propagate along the *c*-direction of elongation. This hypothesis is supported by the previously mentioned fact that the constituent bristles associated with the sheaf-like structure not only possess the same diameter range but also appear to grow along the [001] direction, precisely analogous to the ultrathin Tb-doped $CePO_4$ nanowires collected from the solution. The constituent bristles of the sheaths continually grow at a rate controlled by incident precursor ion diffusion, until they protrude externally from the template pores into solution. It has been previously observed for metals, that growing, elongating nanowires can attain sizes that are significantly greater than the limited ~6 μm length of the template pore channels themselves.[69] Essentially, the nanowires then randomly break, perhaps due to mechanical fracturing[69] as a result of the presence of defects,[70] leading to the isolation of >10 μm long ultrathin nanowires in solution and remnant sheaf-like structures within the template pores themselves.

A summary of our formation mechanism is highlighted in Figure 4. In support of this mechanistic interpretation, we conducted additional reactions. For example, even after a couple of minutes of reagent mixing between the two precursor solutions localized in the two half arms of the U-shaped tube, we could observe the effects of crystal splitting in our product morphology, accompanied by a visual occlusion of the reaction solution medium. Specifically, Supporting Information Figure S4A highlights the sheaf-like bundle morphology of as-obtained nanostructures isolated within the membrane pore channels themselves upon template removal, consistent with the presence of crystal splitting as the first step of our proposed mechanism. Supporting Information Figure S4B is a top-view SEM image taken on the external surface of the template and is suggestive of a plethora of aggregated structures, protruding outward from within individual membrane pores, in agreement with the second step of our formation mechanism. Finally, when we purposely omitted any additional sonication step that might disperse our fractured nanostructures, we note the presence in solution, external to the template, of isolated clusters of nanowire agglomerates, which have retained their initial bundle-like motif, as shown in Supporting Information Figure S4C,D. This expected result, which is compatible with the third step of our protocol, further confirms the plausibility of our crystal splitting formation mechanism.

It is well known that complex morphologies of inorganic materials are usually difficult to produce by simply directly mixing two aqueous solutions of metal salts due to a rapid decrease in supersaturation and further depletion of reaction nutrients within a short period of time.[71] To verify that the pores of the membrane are essential for the directed formation of Tb-doped $CePO_4$ nanostructures, reagent solutions were directly mixed in the absence of a polycarbonate membrane. Neither sheaf-like nanostructures nor ultrathin nanowires were evidently formed. In fact, direct mixing yielded a supersaturated medium and led to the formation of a large number of amorphous, irregular-looking particles (Supporting Information Figure S5). As an experimental observation worthy of note, far fewer nanowires were isolated from the half-cell containing the NaH_2PO_4 solution, suggesting that the diffusion rate of PO_4^{3-} anionic groups was likely faster than that of either Ce^{3+} or Tb^{3+} cations under ambient, acidic reaction conditions. Moreover, after continuous extraction of suspended ultrathin nanowires, we noted that a continuous addition of precursor solutions into the U-tube cells, still separated by a template membrane containing chemically active sheaf-like bundles of nanostructures, resulted in additional, unimpeded production of high-quality, single-crystalline ultrathin nanowires. Our data therefore strongly imply an ambient, green methodology for the large-scale and facile production of lanthanide-doped cerium phosphate nanowires.

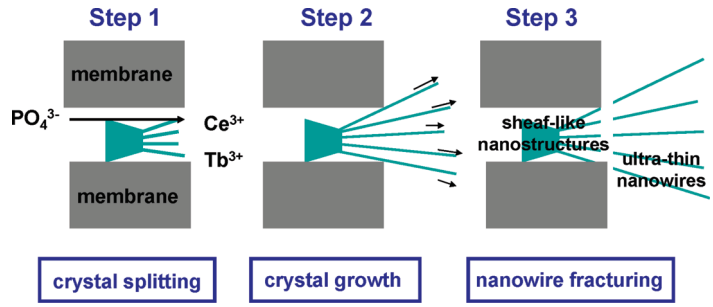

Figure 4. Proposed schematic to account for observed morphologies of ultrathin nanowires and sheaf-like bundles. Step 1: Crystal splitting. Fast growth leads to a metastable state, wherein it becomes thermodynamically favorable for a large crystal to split. Step 2: Selective growth of constituent bristles of sheaf-like bundles along the *c*-axis at a rate controlled by precursor ion diffusion. Step 3: Fragmentation (perhaps due to mechanical instability) of nanowires into ultrathin products that are subsequently isolated in solution.

UV—Visible Spectroscopy and Photoluminescent Activity. The optical properties of our as-prepared ultrathin Tb-doped $CePO_4$ nanowires have been investigated. Cerium-based compounds, such as CeO_2, CeP_2O_7, and $CePO_4$, are known to possess strong absorption for the ultraviolet and have been considered for applications such as tunable sunscreen materials.[72,73] Figure 5 highlights the UV—visible absorption spectrum of thin nanowires collected from solution. A magnified view of the region between 250 and 300 nm is shown as an inset, consisting of a major peak at 278 nm coupled with a number of small shoulder-like features. These bands are overlapping as the excited state is strongly split by the crystal field.[9] Moreover, the results are consistent with reported data for transitions from the ground state $^2F_{5/2}$ ($4f^1$) of Ce^{3+} to the five crystal field split levels of the Ce^{3+} $^2D(5d^1)$ excited states (namely $^2D_{5/2}$ and $^2D_{3/2}$),[9,26] suggesting that useful optical properties were retained in the nanostructured materials.[29] Differences in the spectral behavior between the $CePO_4$ bulk and their nanoscale analogues have often been attributed to the presence of a higher degree of disorder and lattice distortion in the nanowires and the fact that there is a lower crystal field symmetry in these nanowires as compared with the bulk.[26]

The excitation spectrum (λ_{em} = 542 nm) of our as-prepared Tb-doped nanowires is shown in Supporting Information Figure S6, consisting of an intense, broad feature from ~250 to 320 nm with a maximum at 275 nm. Prior reports[10,74–76] have ascribed these bands to allowed f—d transitions from the $^2F_{5/2}$ ground state of Ce^{3+} to different crystal-field components of the 5d level, such as the $^2D_{3/2}$ state.

The black curve in Figure 6 highlights the room-temperature photoluminescent emission spectrum of Tb-doped $CePO_4$ nanowires in water upon excitation at 256 nm (where Tb^{3+} absorption is minimal) at room temperature. The actual doping concentration and inherent density of lanthanide ions are optically significant[74] in terms of governing measured emission inten-

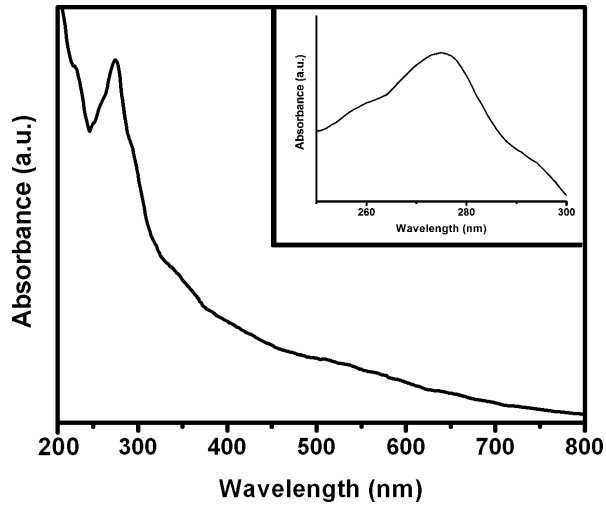

Figure 5. UV−visible spectrum of as-prepared Tb-doped $CePO_4$ nanowires. Expanded region between 250 and 300 nm is shown as an inset.

sities.[10] However, corresponding effects due to particle sizes on the emission signal are expected to be weak, since transitions of the well-shielded f electrons are mainly affected by the local symmetry of the crystal site.[77] Indeed, our data consists of four well-resolved peaks between 450 and 650 nm, corresponding to the $^5D_4-^7F_J$ ($J = 6, 5, 4, 3$) transitions of Tb^{3+} ions. Specifically, these four peaks positioned at 488, 542, 586, and 620 nm can be ascribed to Tb^{3+} emission resulting from $^5D_4-^7F_6$, $^5D_4-^7F_5$, $^5D_4-^7F_4$, and $^5D_4-^7F_3$ relaxations, respectively.[9,78−80] The most intensive peak is located at 542 nm, consistent with the observed bright green luminescence of these samples (Supporting Information, Figure S7).

The broadband between 300 and 400 nm has been previously ascribed to 5d−4f transitions of Ce^{3+}. Owing to the relatively high concentration of Ce^{3+} in the nanowires, the excited state of Ce^{3+} is not completely quenched by energy transfer to Tb^{3+}.[10,30] In fact, the nature of the observed photoluminescence is dependent upon the probability of energy transfer through the host cerium lattice (governed by factors such as electric dipole−dipole interaction and reabsorption of emission) as well as the probability of energy transfer from the lattice to the Tb^{3+} "activator".[81,82] The intrinsic emission of Ce^{3+}, associated with two transitions from the lowest component of the ^2D state to the spin−orbit components of the ground state, $^2F_{7/2}$ and $^2F_{5/2}$,[77] is a broadband. By contrast, the absorption of Tb^{3+} consists of narrow lines.[14] The expected energy transfer process between Ce^{3+} and Tb^{3+} is schematically depicted in Supporting Information Figure S8, wherein energy transfer takes place from the $^5D_{3/2}$ state of the Ce^{3+} "sensitizer" to the acceptor states of Tb^{3+}, which decay nonradiatively to the $^5D_4$ and $^5D_3$ states followed by a radiative decay process to lower levels of ^7F_J ($J = 0-6$).[9]

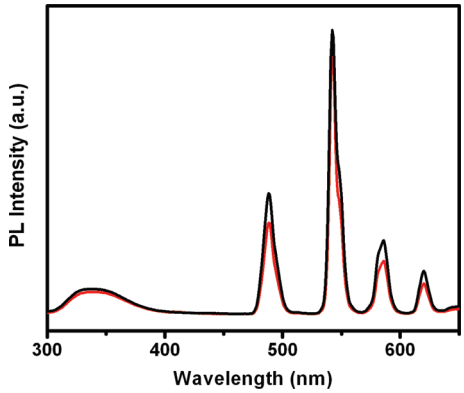

Figure 6. Photoluminescence spectra, obtained upon excitation at 256 nm at room temperature, of as-prepared Tb-doped $CePO_4$ nanowires before (black curve) and after (red curve) five successive redox cycles.

However, efficient energy transfer between cerium and terbium is possible only between nearest neighbors in the crystal lattice and when there is optimal spectral overlap.[83] Therefore, if there is radiative transfer, some narrow dips at the location of Tb^{3+} absorption lines would appear to be associated with an emission intensity decrease[14] but the depression of the entire cerium emission spectrum would not occur. This incomplete energy transfer from Ce^{3+} to Tb^{3+} has been observed for bulk analogues as well as for other Ce-based matrices.[14,81,84]

Photoluminescence switching behavior (Supporting Information Figure S7) has been previously observed in these systems,[9,10,84] related to dramatic changes in the emission intensity of Tb^{3+}, upon oxidation and reduction processes. Specifically, upon addition of $KMnO_4$ to the as-prepared colloidal dispersion of Tb-doped $CePO_4$ nanowires, Ce^{3+} was oxidized to Ce^{4+}, essentially suppressing the observed emission entirely. Subsequent reduction of Ce^{4+} to Ce^{3+} through the addition of ascorbic acid ($C_6H_8O_6$) to the oxidized nanowire solution effectively restored the observed luminescence to its original profile.

As shown in Figure 6 and Supporting Information, Figure S7, the switching process is reversible. That is, the photoluminescence spectra of as-prepared Tb-doped $CePO_4$ nanowires (black curve) and of samples taken after five successive redox cycles (red curve) are shown in which the luminescence of these nanostructures was repeatedly quenched ("off" state) by oxidation with $KMnO_4$ followed by its recovery ("on" state) upon reduction with ascorbic acid. The emission profiles are essentially identical with only a slight degradation in luminescence intensity with no apparent change in nanowire morphology (Supporting Information, Figure S9). In fact, the ratio of luminescence intensities taken of the nanowire samples before and immediately after five successive $KMnO_4$/ascorbic acid redox cycles was as much as 95% at the 542 nm emission peak. These results demonstrate that our as-prepared ultrathin Tb-doped $CePO_4$ nanowires are robust and the reproducible change in luminescence signal can theoretically be used to as a sensitive and rapid

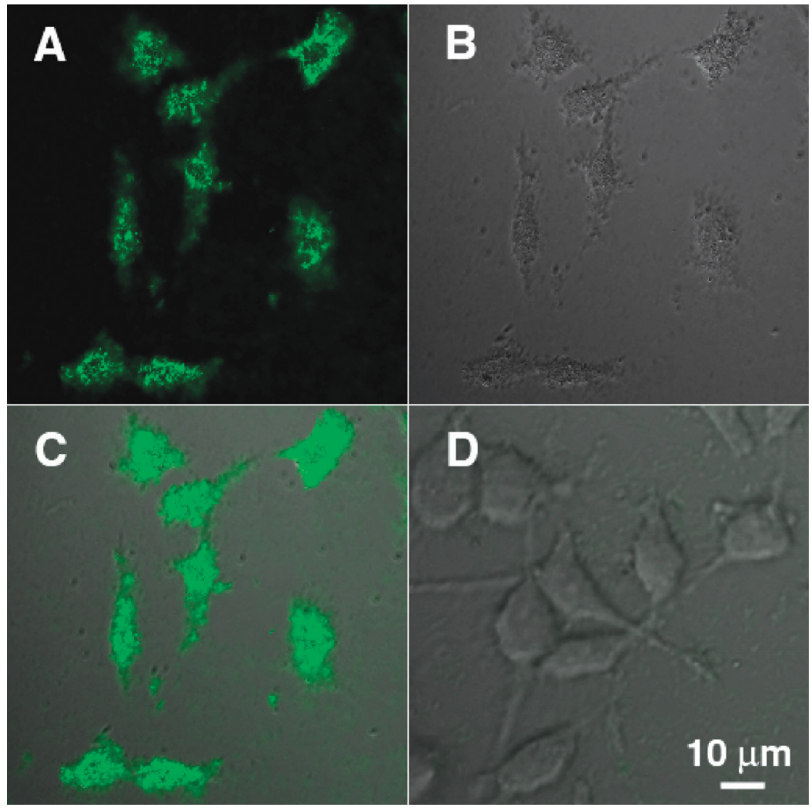

Figure 7. Confocal fluorescence microscopy images of HeLa cells: (A) confocal luminescence images of cells taken after incubation with 0.2 mg/mL of Tb-doped $CePO_4$ nanowires for 2 h at 37 °C; (B) bright-field optical image of cells shown in panel A; (C) overlay image of both panels A and B; (D) corresponding overlay image of cells obtained after incubation with 0.2 mg/mL of Tb-doped $CePO_4$ nanowires for 2 h at 4 °C.

indicator of the redox behavior of their surrounding environments. Moreover, owing to their reported low toxicity[9] and reasonable dispersibility in cell culture medium (up to as much as 0.5 mg/mL for a period of 2 days), these nanostructures are potentially viable candidates for biological labels and probes.

Biocompatibility and Potential for Bioimaging. Generally, the cellular permeability and cytotoxicity characteristics of fluorescent nanomaterials are critical to their application as luminescent biological labels. It has already been established that inorganic fluorescent lanthanide (europium and terbium) orthophosphate (*e.g.*, $EuPO_4 \cdot H_2O$ and $TbPO_4 \cdot H_2O$) nanorods, synthesized by a microwave technique, can behave as biolabels and can be internalized into either human umbilical vein endothelial cells, 786-O cells, or renal carcinoma cells, though the exact mechanism for their internalization remained unclear.[85,86] Hence, to confirm the potential applicability of our ultrathin green luminescent Tb-doped $CePO_4$ nanowires in a biological system, we conducted analogous experiments using HeLa cells measuring 12−20 μm in diameter. To facilitate processing, prior to cellular incubation, our as-prepared thin, long nanowires were sonicated for ~1 h in order to generate noticeably shorter structures (Supporting Information, Figure S10), measuring 3.2 ± 2 μm in length.

As a control experiment, HeLa cells alone showed negligible background fluorescence under two-photon excitation. Nonetheless, upon incubation, incorporation of cut, as-prepared Tb-doped $CePO_4$ nanowires into HeLa cells was confirmed by confocal fluorescence microscopy. Specifically, after incubation with 0.2 mg/mL of Tb-doped $CePO_4$ nanowires for 2 h at 37 °C, an intense intracellular luminescence was observed, as shown in Figure 7A. These inorganic phosphate nanowires clearly retained their intrinsic fluorescent properties upon cellular internalization. Moreover, the corresponding bright-field measurements taken after treatment with the nanowires confirmed that the cells were viable throughout the imaging experiments (Figure 7B) and that there were no evident regions of cell death. As indicated in Figure 7C, overlays of both confocal luminescence and bright-field images further demonstrated that the observed luminescence was noticeable throughout the entire intracellular region, thereby strongly suggesting that the nanowires were internalized into the cells themselves as opposed to merely staining the external membrane surface.[87]

To confirm the spatial localization of nanowires within a typical cell, we obtained a series of Z-stack images of the cell (*e.g.*, top to bottom) at 1 μm "slice" intervals of an individual HeLa cell stained with Tb-doped $CePO_4$ nanowires. Data associated with the middle, central slice

(Supporting Information, Figure S11), corresponding to orthogonal *xy*, *yz*, and *xz* planes, respectively, are shown. Because these three planes share a common focal center within the cell itself and moreover, as these intimately interconnected planes evidently all demonstrate green fluorescence simultaneously, we can reasonably conclude that the fluorescently doped lanthanide nanowires are localized within the interior environment of the HeLa cells themselves.

We noted a dramatic decrease in the fluorescence intensity in data taken after identical cellular incubation with our as-prepared Tb-doped $CePO_4$ nanowires at the same concentrations, but at a noticeably lower temperature (*i.e.*, 4 °C), as compared with that observed in cells treated with nanowires at 37 °C. The overlap image (Figure 7D) suggests that there was little if any nanowire incorporation.

Overall, these data are consistent with our prior work on oxidized single-walled carbon nanotubes (SWNTs), wherein their internalization into HeLa cells involved a temperature-dependent diffusion process akin to a "pierce-through" mechanism.[88] That is, these SWNTs tended to act as nanoneedles that could pierce through cell membranes, thereby allowing for their diffusion into cells.[89] Since our lanthanide nanowires were not specifically functionalized with biologically relevant surface functional groups, we do not have sufficient evidence to unequivocally conclude that receptor-mediated endocytosis played a dominant role in the observed cellular internalization.

Our experiments were conducted in cell culture media and interestingly, it has been recently reported[90,91] that serum proteins from biological media, such as bovine serum albumin (BSA), can nonspecifically coat the surfaces of gold nanorods, leading to all nanorod samples bearing the same effective charge, regardless of their initial surface charge. In that system,[90,91] it was proposed that externally adsorbed BSA facilitated the uptake of nanorods into human cancer cells, such as either HeLa or HT-29, *via* receptor-mediated endocytosis arising from cellular recognition of these proteins. It is very plausible to imagine an analogous scenario herein, especially since BSA has been previously noted[92,93] to be able to nonspecifically adsorb onto a diverse range of different surfaces, functionalized or not.

Nonetheless, our results confirm that as-prepared Tb-doped $CePO_4$ nanowires can viably be used as fluorescent labels for biological imaging. We also incubated our HeLa cells with different concentrations (ranging from 0.1 to 0.5 mg/mL) and time periods (from 2 to 24 h) of as-prepared Tb-doped $CePO_4$ nanowires in order to test their inherent sensitivity as luminescent probes. Representative CFM images are shown in Supporting Information Figure S12A−C. An analysis of the corresponding CFM intensities, proportional to the number of doped phosphate nanowires internalized by the HeLa cells, in Figure 8 panels A and B demonstrates an increase in the measured fluorescence, with increasing nanowire concentrations and cellular incubation periods, as expected. Our data show that even nanowire concentrations as low as 0.1 mg/mL and incubation times as short as 2 h can yield sufficient nanowire integration into HeLa cells so as to generate sufficiently strong fluorescence for bioimaging purposes.

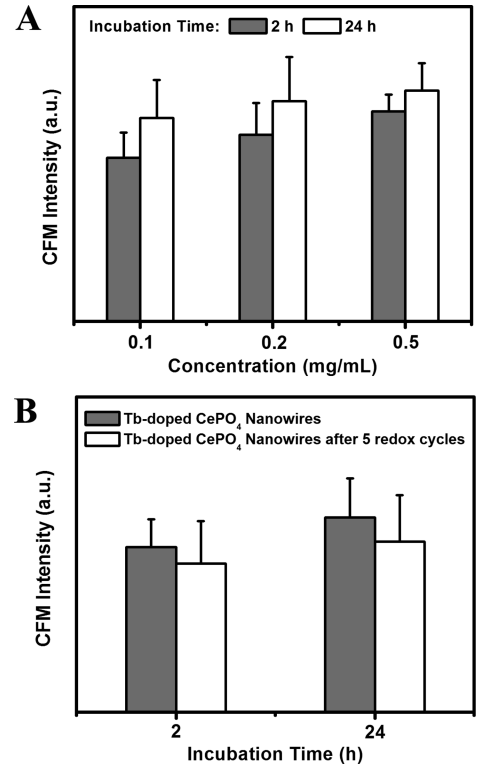

Figure 8. Statistical analysis pertaining to CFM intensity of HeLa cells after incubation with (A) as-prepared Tb-doped $CePO_4$ nanowires at different concentrations for periods of 2 and 24 h, respectively; (B) 0.2 mg/mL as-prepared Tb-doped $CePO_4$ nanowires for 2 and 24 h, respectively, before and after redox cycles.

Furthermore, Tb-doped $CePO_4$ nanowires, subjected to repeated redox cycles, were also incubated with HeLa cells. The degree of cellular uptake was analogously confirmed by CFM data. Specifically, "oxidized" nanowires did not evince any fluorescence within cells, whereas cells treated with "reduced" nanowires demonstrated a measurable degree of fluorescence (Supporting Information Figure S12D). Quantitatively, as compared with as-prepared nanowires, there was a small decrease (7%−13%) in the fluorescence intensity measured in cells. This value was comparable in magnitude to the decrease observed in pure nanowire suspensions, as measured by PL spectroscopy (Figure 6).

Moreover, to verify whether these ultrathin Tb-doped $CePO_4$ nanowires are biologically nontoxic and biocompatible, cytotoxicity studies of HeLa cells were performed, based on the reduction activity of methyl thiazolyl tetrazolium (MTT), and are shown in Figure 9, based on previous analogous work.[87] The viability of untreated cells was assumed to be 100%. Upon incuba-

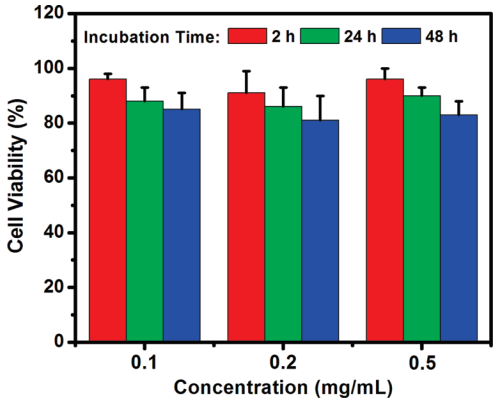

Figure 9. ***In vitro*** **cell viability of HeLa cells incubated with Tb-doped $CePO_4$ nanowires at different concentrations for periods ranging from 2 to 48 h.**

tion of HeLa cells with a 0.1 mg/mL solution of Tb-doped $CePO_4$ nanowires, we noted that fewer than 15% of the cells died after a 48 h exposure. When the concentration of nanowires was increased to 0.5 mg/mL, the observed cell viability still remained above 80%, again after 48 h of exposure. Therefore, these data strongly suggested that ultrathin Tb-doped $CePO_4$ nanowires can be considered to possess reasonably low cytotoxicity, which is in agreement with previous reports that rare-earth-based nanophosphors maintain decent chemical stability and generally low toxicity, which are essential for legitimate bioimaging applications.[87,94]

CONCLUSIONS

A simple, effective, and versatile template-directed method has been developed for the successful large-scale preparation of ultrathin Tb-doped $CePO_4$ nanowires possessing very high-aspect ratios, under ambient room temperature conditions. Sheaf-like bundles of 1D nanostructures may initially form through a crystal splitting growth mechanism, followed by continuous growth out of template membrane pore channels, until they finally fracture in solution. This new synthetic approach is important not only because it involves a number of intriguing fundamental steps, but also because this environmentally benign route can be readily extended to the synthesis of other kinds of rare-earth phosphate nanomaterials either with or without dopants. The resulting Tb-doped $CePO_4$ nanowires displayed a redox-switchable green photoluminescence that was subsequently exploited for biological labeling purposes. Moreover, we noted that our nanostructures not only were biocompatible with cells but also were relatively nontoxic over reasonable incubation time periods and concentrations, of significance for applications in biomedical diagnostics and analyses

EXPERIMENTAL SECTION

Synthesis. Polycarbonate track-etched membranes, measuring ca. 6 μm in thickness, can contain pore sizes of either 15, 50, 100, or 200 nm diameter, and were purchased from Whatman Co., UK. The membranes were initially hydrated by immersion and sonication in a small volume of distilled, deionized water for a few minutes, so as to limit the formation of air bubbles either within their interior pore structures or on their exterior surfaces. Subsequently, the membrane was mounted between two half arms of a U-shaped tube. In a typical ambient synthesis, one of the two half cells was filled with a 0.01 M NaH_2PO_4 (Fisher Scientific; 99.1%) solution, which was adjusted to acidic reaction conditions (*e.g.*, pH values from 2 to 6) using HCl, and the other half cell contained a solution by mixing 0.05 M $CeCl_3$ (Aldrich, 99.9%) solution together with $Tb(NO_3)_3$ (Alfa Aesar, 99.9%) up to a final molar concentration of 10.0%, so as to generate desired Tb-doped $CePO_4$ nanostructures. The system was then left unperturbed for an incubation period of only 2 h at room temperature. It is noteworthy that varying the concentrations of NaH_2PO_4 from 0.001 to 0.05 M and of $CeCl_3$ from 0.005 to 0.25 M (with the Tb content adjusted to provide for a final molar concentration of 10.0%) yielded essentially identical results in terms of ultimate product morphology. Subsequent to immersion, the half cell containing both $CeCl_3$ and $Tb(NO_3)_3$ solutions became occluded in nature, and a white precipitate was obtained after centrifugation. To isolate products within the template itself, the polycarbonate membrane was detached, sonicated for about 2 min to remove the unwanted particles on the surface, and thoroughly washed with distilled water, before being dissolved again with methylene chloride. As-prepared phosphate nanostructures were isolated from solution by centrifugation upon washing.

Characterization. As-prepared samples were thoroughly characterized using a number of different methodologies, including powder X-ray diffraction (XRD), field-emission scanning electron microscopy (FE-SEM), transmission electron microscopy (TEM), high resolution TEM (HRTEM), selected area electron diffraction (SAED), and energy-dispersive X-ray spectroscopy (EDS), as well as with UV−visible and photoluminescence (PL) spectroscopies.

X-ray Diffraction. Crystallographic and purity information on the as-prepared phosphate nanostructures were initially obtained using powder X-ray diffraction (XRD). To prepare samples, the resulting nanowire samples were rendered into slurries in ethanol, sonicated for about 1 min, and then air-dried upon deposition onto glass slides. Diffraction patterns were subsequently collected using a Scintag diffractometer, operating in the Bragg configuration using Cu K*a* radiation ($\lambda = 1.54$ Å) ranging from 10 to 80° at a scanning rate of 2° per minute.

Electron Microscopy. The morphology and size distribution of the resulting phosphate nanowires were initially characterized using a field emission SEM (FE-SEM Leo 1550) at accelerating voltages of 15 kV and equipped with EDS capabilities. Specifically, samples for SEM were prepared by dispersing as-prepared phosphate nanowires in ethanol, sonicating for about 2 min, and then depositing them onto a silicon wafer, attached to a SEM brass stub using conductive carbon tape. All of these samples were subsequently conductively coated with gold by sputtering for 15 s so as to minimize charging effects under SEM imaging conditions.

Low magnification transmission electron microscopy (TEM) images were taken at an accelerating voltage of 80 kV on a FEI Tecnai12 BioTwinG^2 instrument, equipped with an AMT XR-60 CCD digital camera system. High-resolution transmission electron microscopy (HRTEM) images and SAED patterns were obtained on a JEOL 2010F instrument at accelerating voltages of 200 kV. Specimens for all of these TEM experiments were prepared by dispersing the as-prepared product in ethanol, sonicating for 2 min to ensure adequate dispersion of the nanowires, and dipping one drop of the solution onto a 300 mesh Cu grid, coated with a lacey carbon film.

Optical Spectroscopy. UV−visible spectra were collected at high resolution on a Thermospectronics UV1 spectrometer using quartz cells with a 10-mm path length. Spectra were obtained for as-prepared phosphate nanorods, which were then sonicated

in distilled water so as to yield homogeneous dispersions. UV−visible absorption spectra were recorded using distilled water as a blank.

Samples for PL spectra were dispersed in deionized water and sonicated for 1 min. Fluorescence data were subsequently obtained at room temperature on a Jobin Yvon Spex FluoroMax-4 with a 10 s integration time, using an excitation wavelength of 256 nm.

To test luminescence switching behavior, $KMnO_4$ and ascorbic acid were used to oxidize and reduce Ce^{3+}, respectively, in each cycle. As-treated samples were washed by water several times in order to eliminate impurities prior to measurement.

Biological Experiments. We tested the viability of as-prepared Tb^{3+}-doped cerium phosphate nanowires as fluorescent biological labels for *in vitro* bioimaging. We should mention that prior to processing, our Tb-doped $CePO_4$ nanowires were sonicated for about 1 h in order to shorten their lengths so as to assist their biological incorporation.

Cell Culture. [95,96] Human cervical cancer (HeLa) cells were initially propagated onto 100 mm-diameter tissue culture dishes in DMEM medium (Life Technologies, GIBCO), supplemented with 10% fetal bovine serum (FBS) at 37 °C in a humidified atmosphere containing 5% CO_2. At confluence, the cells were washed, trypsinized, and resuspended in culture medium.

Cellular Uptake. [95,96] HeLa cells were seeded at a concentration of 10^4 cells/well on 12 mm-diameter glass coverslips in 24-well tissue culture plates, and allowed to grow for 24 h at 37 °C under 5% CO_2. Nanowires were subsequently added at different concentrations ranging from 0.1 to 0.5 mg/mL into the culture medium, and cells were grown for either an additional 2 or 24 h at 37 °C under a 5% CO_2 atmosphere. Subsequently, the cell medium was removed, and cells on the coverslips were washed with phosphate buffered saline (PBS) three times so as to clear free nanowires from both the medium and the cell surface, prior to imaging.

Confocal Microscopy (CFM) Imaging. Cells treated as described above were resuspended in 100 μL of PBS after each experiment, and dropped onto an uncoated bottom glass dish (MatTek Corp.). CFM experiments aimed at assessing cellular uptake, localization, and fluorescent signaling of the nanowires were subsequently performed using a Zeiss LSM 510 META NLO two-photon laser scanning confocal microscope system, operating at around a 380 nm excitation wavelength using a tunable Chameleon XR laser system and a 505 nm long-pass filter. Images were captured using either a C-Apochromat 63 × /1.2 Water (corr.) objective or a Plan-Apochromat 100 × /1.45 oil objective. Acquired data were analyzed using the LSM 510 META software. Orthogonal sectioning images were recorded within the cells by focusing on the *xy* plane along the *z* axis, the *yz* plane along the *x* axis, and the *xz* plane along the *y* axis, respectively.

Cell Cytotoxicity. [96] A tetrazolium salt, 3-(4,5-dimethylthiazol-2-yl)-2,5-diphenyltetrazolium bromide (MTT), assay of HeLa cells was performed to test the cytotoxicity of as-prepared products. In this assay, cells were seeded in a 96-well microplate at a density of 5000 cells per well. After 24 h of incubation, the nanowires were directly added to the culture medium at different concentrations ranging from 0.1 to 0.5 mg/mL, and the plate was incubated for another additional 2 to 48 h at 37 °C. At the end of the cell culture incubation, MTT was added into each well. After processing for 4 h, all media were removed and acidic ethanol was added to each well before absorbance was measured by a microplate reader. The following formula was used to calculate the degree of inhibition of cell growth: cell viability (%) = ((mean of absorbance value of treatment group)/(mean absorbance value of control)) × 100.[87]

Acknowledgment. We acknowledge the U.S. Department of Energy (DE-AC02-98CH10886) for facility and personnel support. We also thank the National Science Foundation (CAREER Award DMR-0348239), and the Alfred P. Sloan Foundation for PI support and experimental supplies. Moreover, we are grateful to D. Wang (Boston College) as well as to J. Quinn (SUNY Stony Brook) for their assistance with electron microscopy. The authors also acknowledge the technical service and advice provided by S. Van Horn for TEM and G-W. Tian for CFM, performed at the Central Microscopy Imaging Center at Stony Brook. We also thank M. Das and R. Rowehl for their valuable help with cell culture preparations at the Cell Culture and Hybridoma facility at Stony Brook.

Supporting Information Available: Figures S1−S12 as described in the text. This material is available free of charge *via* the Internet at http://pubs.acs.org.

REFERENCES AND NOTES

1. De, M.; Ghosh, P. S.; Rotello, V. M. Applications of Nanoparticles in Biology. *Adv. Mater.* **2008**, *20*, 4225–4241.
2. Chan, W. C. W.; Nie, S. Quantum Dot Bioconjugates for Ultrasensitive Nonisotopic Detection. *Science* **1998**, *281*, 2016–2018.
3. Bruchez, M.; Moronne, M.; Gin, P.; Weiss, S.; Alivisatos, A. P. Semiconductor Nanocrystals as Fluorescent Biological Labels. *Science* **1998**, *281*, 2013–2016.
4. Larson, D. R.; Zipfel, W. R.; Williams, R. M.; Clark, S. W.; Bruchez, M. P.; Wise, F. W.; Webb, W. W. Water-Soluble Quantum Dots for Multiphoton Fluorescence Imaging *in Vivo*. *Science* **2003**, *300*, 1434–1436.
5. Mondejar, S. P.; Kovtun, A.; Epple, M. Lanthanide-Doped Calcium Phosphate Nanoparticles with High Internal Crystallinity and with a Shell of DNA as Fluorescent Probes in Cell Experiments. *J. Mater. Chem.* **2007**, *17*, 4153–4159.
6. Meiser, F.; Cortez, C.; Caruso, F. Biofunctionalization of Fluorescent Rare-Earth-Doped Lanthanum Phosphate Colloidal Nanoparticles. *Angew. Chem., Int. Ed.* **2004**, *43*, 954–5957.
7. Wang, L.; Qian, B.; Chen, H.; Liu, Y.; Liang, A. A Novel Efficient Fret System: $CePO_4$:Tb^{3+} Nanocrystal as Donor and Rhodamine B Dye as Acceptor. *Chem. Lett.* **2008**, *37*, 402–403.
8. Zhang, Y.-W.; Sun, X.; Si, R.; You, L.-P.; Yan, C.-H. Single-Crystalline and Monodisperse LaF_3 Triangular Nanoplates from a Single-Source Precursor. *J. Am. Chem. Soc.* **2005**, *127*, 3260–3261.
9. Li, Q.; Yam, V. W.-W. Redox Luminescence Switch Based on Energy Transfer in $CePO_4$:Tb^{3+} Nanowires. *Angew. Chem., Int. Ed.* **2007**, *46*, 3486–3489.
10. Chen, G.; Sun, S.; Zhao, W.; Xu, S.; You, T. Template Synthesis and Luminescence Properties of $CePO_4$:Tb Nanotubes. *J. Phys. Chem. C* **2008**, *112*, 20217–20221.
11. Di, W.; Wang, X.; Zhu, P.; Chen, B. Energy Transfer and Heat-Treatment Effect of Photoluminescence in Eu^{3+}-Doped $TbPO_4$ Nanowires. *J. Solid State Chem.* **2007**, *180*, 467–473.
12. Huignard, A.; Gacoin, T.; Boilot, J.-P. Synthesis and Luminescence Properties of Colloidal YVO_4:Eu Phosphors. *Chem. Mater.* **2000**, *12*, 1090–1094.
13. Di, W.; Zhao, X.; Lu, S.; Wang, X.; Zhao, H. Thermal and Photoluminescence Properties of Hydrated YPO_4:Eu^{3+} Nanowires. *J. Solid State Chem.* **2007**, *180*, 2478–2484.
14. Shionoya, S.; Nakazawa, E. Sensitization of Tb^{3+} Luminescence by Ce^{3+} and Cu^{+} in Glasses. *Appl. Phys. Lett.* **1965**, *6*, 118–120.
15. Yin, Y.; Alivisatos, A. P. Colloidal Nanocrystal Synthesis and the Organic−Inorganic Interface. *Nature* **2005**, *437*, 664–670.
16. Rajesh, K.; Shajesh, P.; Pullithadathil, B.; Warrier, K. G. High Surface Area Mesoporous Nanocrystalline Lanthanum Phosphate Nanorod through a Sol-Gel Process—Effect of Alcohol Washing on a Non-oxide Gel. *Microporous Mesoporous Mater.* **2008**, *116*, 693–697.
17. Hou, Z.; Yang, P.; Li, C.; Wang, L.; Lian, H.; Quan, Z.; Lin, J. Preparation and Luminescence Properties of YVO_4:Ln and Y(V, P)PO_4:Ln (Ln = Eu^{3+}, Sm^{3+}, Dy^{3+}) Nanofibers and Microbelts by Sol-Gel/Electrospinning Process. *Chem. Mater.* **2008**, *20*, 6686–6696.
18. Xu, L.; Song, H.; Dong, B.; Wang, Y.; Bai, X.; Wang, G.; Liu, Q. Electrospinning Preparation and Photoluminescence Properties of Lanthanum Phosphate Nanowires and Nanotubes. *J. Phys. Chem. C* **2009**, *113*, 9609–9615.

19. Fang, Y.-P.; Xu, A.-W.; Qin, A.-M.; Yu, R.-J. Selective Synthesis of Hexagonal and Tetragonal Dysprosium Orthophosphate Nanorods by a Hydrothermal Method. *Cryst. Growth Des.* **2005**, *5*, 1221–1225.
20. Cao, M.; Hu, C.; Wu, Q.; Guo, C.; Qi, Y.; Wang, E. Controlled Synthesis of $LaPO_4$ and $CePO_4$ Nanorods/Nanowires. *Nanotechnology* **2005**, *16*, 282–286.
21. Yu, L.; Li, D.; Yue, M. Fabrication and Characterization of the Photoluminescent Properties of Tb^{3+} Doped One-Dimensional $GdPO_4$ Nanorods. *Mater. Lett.* **2007**, *61*, 4374–4376.
22. Lam, W. M.; Wong, C. T.; Li, Z. Y.; Luk, K. D. K.; Chan, W. K.; Yang, C.; Chiu, K. Y.; Xu, B.; Lu, W. W. Solvothermal Synthesis of Strontium Phosphate Chloride Nanowire. *J. Cryst. Growth* **2007**, *306*, 129–134.
23. Yan, R.; Sun, X.; Wang, X.; Peng, Q.; Li, Y. Crystal Structures, Anisotropic Growth, and Optical Properties: Controlled Synthesis of Lanthanide Orthophosphate One-Dimensional Nanomaterials. *Chem.—Eur. J.* **2005**, *11*, 2183–2195.
24. Chen, G.-Y.; Qu, W.-G.; Ye, F.; Zhang, W.-X.; Xu, A.-W. Hydrothermal Synthesis of Ferroelectric $PbHPO_4$ Nanowires from a Single-Source Precursor. *J. Phys. Chem. C* **2008**, *112*, 16818–16823.
25. Zheng, Y.; Cheng, Y.; Wang, Y.; Yu, Y.; Chen, D.; Bao, F. Selective-Controlled Synthesis of One-Dimensional Strontium Phosphates. *J. Cryst. Growth* **2005**, *280*, 569–574.
26. Fang, Y.-P.; Xu, A.-W.; Song, R.-Q.; Zhang, H.-X.; You, L.-P.; Yu, J. C.; Liu, H.-Q. Systematic Synthesis and Characterization of Single-Crystal Lanthanide Orthophosphate Nanowires. *J. Am. Chem. Soc.* **2003**, *125*, 16025–16034.
27. Yan, Z.-G.; Zhang, Y.-W.; You, L.-P.; Si, R.; Yan, C.-H. Controlled Synthesis and Characterization of Monazite-Type Monocrystalline Nanowires of Mixed Lanthanide Orthophosphates. *Solid State Commun.* **2004**, *130*, 125–129.
28. Yu, L.; Song, H.; Lu, S.; Liu, Z.; Yang, L.; Kong, X. Luminescent Properties of $LaPO_4$:Eu Nanoparticles and Nanowires. *J. Phys. Chem. B* **2004**, *108*, 16697–16702.
29. Xing, Y.; Li, M.; Davis, S. A.; Mann, S. Synthesis and Characterization of Cerium Phosphate Nanowires in Microemulsion Reaction Media. *J. Phys. Chem. B* **2006**, *110*, 1111–1113.
30. Zhu, L.; Liu, X.; Liu, X.; Li, Q.; Li, J.; Zhang, S.; Meng, J.; Cao, X. Facile Sonochemical Synthesis of $CePO_4$:Tb/$LaPO_4$ Core/Shell Nanorods with Highly Improved Photoluminescent Properties. *Nanotechnology* **2006**, *17*, 4217–4222.
31. Xia, Y.; Yang, P.; Sun, Y.; Wu, Y.; Mayers, B.; Gates, B.; Yin, Y.; Kim, F.; Yan, H. One-Dimensional Nanostructures: Synthesis, Characterization, and Applications. *Adv. Mater.* **2003**, *15*, 353–389.
32. Schmid, G. Materials in Nanoporous Alumina. *J. Mater. Chem.* **2002**, *12*, 1231–1238.
33. Hulteen, J. C.; Martin, C. R. A General Template-Based Method for the Preparation of Nanomaterials. *J. Mater. Chem.* **1997**, *7*, 1075–1087.
34. Lakshmi, B. B.; Dorhout, P. K.; Martin, C. R. Sol−Gel Template Synthesis of Semiconductor Nanostructures. *Chem. Mater.* **1997**, *9*, 857–862.
35. Limmer, S. J.; Seraji, S.; Wu, Y.; Chou, T. P.; Nguyen, C.; Cao, G. Template-Based Growth of Various Oxide Nanorods by Sol−Gel Electrophoresis. *Adv. Funct. Mater.* **2002**, *12*, 59–64.
36. Mao, Y.; Wong, S. S. A General, Room-Temperature Method for the Synthesis of Isolated as Well as Arrays of Single-Crystalline ABO_4-Type Nanorods. *J. Am. Chem. Soc.* **2004**, *126*, 15245–15252.
37. Mao, Y.; Zhang, F.; Wong, S. S. Ambient Template-Directed Synthesis of Single-Crystalline Alkaline Earth Metal Fluoride Nanowires. *Adv. Mater.* **2006**, *18*, 1895–1899.
38. Zhou, H.; Wong, S. S. A Facile and Mild Synthesis of 1-D ZnO, CuO, and α-Fe_2O_3 Nanostructures and Nanostructured Arrays. *ACS Nano* **2008**, *2*, 944–958.
39. Zhou, H.; Yiu, Y.; Aronson, M. C.; Wong, S. S. Ambient Template Synthesis of Multiferroic $MnWO_4$ Nanowires and Nanowire Arrays. *J. Solid State Chem.* **2008**, *181*, 1539–1545.
40. Zhang, F.; Mao, Y.; Park, T.-J.; Wong, S. S. Green Synthesis and Property Characterization of Single-Crystalline Perovskite Fluoride Nanorods. *Adv. Funct. Mater.* **2008**, *18*, 103–112.
41. Zhang, F.; Sfeir, M. Y.; Misewich, J. A.; Wong, S. S. Room-Temperature Preparation, Characterization, and Photoluminescence Measurements of Solid Solutions of Various Compositionally-Defined Single-Crystalline Alkaline-Earth-Metal Tungstate Nanorods. *Chem. Mater.* **2008**, *20*, 5500–5512.
42. Zhang, F.; Yiu, Y.; Aronson, M. C.; Wong, S. S. Exploring the Room-Temperature Synthesis and Properties of Multifunctional One-Dimensional Doped Tungstate Nanorods. *J. Phys. Chem. C* **2008**, *112*, 14816–14824.
43. Murphy, K. E.; Altman, M. B.; Wunderlich, B. The Monoclinic-to-Trigonal Transformation in Selenium. *J. Appl. Phys.* **1977**, *48*, 4122–4131.
44. Stavila, V.; Whitmire, K. H.; Rusakova, I. Synthesis of Bi_2S_3 Nanostructures from Bismith(III) Thiourea and Thiosemicarbazide Complexes. *Chem. Mater.* **2009**, *21*, 5456–5465.
45. Peng, Z. A.; Peng, X. G. Mechanisms of the Shape Evolution of CdSe Nanocrystals. *J. Am. Chem. Soc.* **2001**, *123*, 1389–1395.
46. Peng, Z. A.; Peng, X. G. Nearly Monodisperse and Shape-Controlled CdSe Nanocrystals *via* Alternative Routes: Nucleation and Growth. *J. Am. Chem. Soc.* **2002**, *124*, 3343–3353.
47. Zhang, Y.; Guan, H. Hydrothermal Synthesis and Characterization of Hexagonal and Monoclinic $CePO_4$ Single-Crystal Nanowires. *J. Cryst. Growth* **2003**, *256*, 156–161.
48. Hu, W.; Zhao, Y.; Liu, Z.; Dunnill, C. W.; Gregory, D. H.; Zhu, Y. Nanostructural Evolution: From One-Dimensional Tungsten Oxide Nanowires to Three-Dimensional Ferberite Flowers. *Chem. Mater.* **2008**, *20*, 5657–5665.
49. Okada, A.; Yoshimura, M.; Ueda, K. Fabrication of Comblike Nanostructures Using Self-Assembled Cluster Arrays of Molybdenum Oxides. *Appl. Phys. Lett.* **2007**, *90*, 203102-1–203102-3.
50. Dai, Q.; Xiao, N.; Ning, J.; Li, C.; Li, D.; Zou, B.; Yu, W. W.; Kan, S.; Chen, H.; Liu, B.; Zou, G. Synthesis and Mechanism of Particle- and Flower-Shaped ZnSe Nanocrystals: Green Chemical Approaches toward Green Nanoproducts. *J. Phys. Chem. C* **2008**, *112*, 7567–7571.
51. Zitoun, D.; Pinna, N.; Frolet, N.; Belin, C. Single-Crystal Manganese Oxide Multipods by Oriented Attachment. *J. Am. Chem. Soc.* **2005**, *127*, 15034–15035.
52. Hu, Y.; Chen, K. Crystal Splitting in the Growth of β-FeO(OH). *J. Cryst. Growth* **2007**, *308*, 185–188.
53. Kelly, A. T.; Rusakova, I.; Ould-Ely, T.; Hofmann, C.; Luttge, A.; Whitmire, K. H. Iron Phosphide Nanostructures Produced from a Single-Source Organometallic Precursor: Nanorods, Bundles, Crosses, and Spherulites. *Nano Lett.* **2007**, *7*, 2920–2925.
54. Tang, J.; Alivisatos, A. P. Crystal Splitting in the Growth of Bi_2S_3. *Nano Lett.* **2006**, *6*, 2701–2706.
55. Li, L.; Sun, N.; Huang, Y.; Qin, Y.; Zhao, N.; Gao, J.; Li, M.; Zhou, H.; Qi, L. Topotactic Transformation of Single-Crystalline Precursor Discs into Disc-Like Bi_2S_3 Nanorod Networks. *Adv. Funct. Mater.* **2008**, *18*, 1194–1201.
56. Shen, X.-F.; Yan, X.-P. Facile Shape-Controlled Synthesis of Well-Aligned Nanowire Architectures in Binary Aqueous Solution. *Angew. Chem., Int. Ed.* **2007**, *46*, 7659–7663.
57. Deng, H.; Liu, C.; Yang, S.; Xiao, S.; Zhou, Z.-K.; Wang, Q.-Q. Additive-Mediated Splitting of Lanthanide Orthovanadate Nanocrystals in Water: Morphological Evolution from Rods to Sheaves and to Spherulites. *Cryst. Growth Des.* **2008**, *8*, 4432–4439.

58. Kim, S.; Lee, J. S.; Mitterbauer, C.; Ramasse, Q. M.; Sarahan, M. C.; Browning, N. D.; Park, H. J. Anomalous Electrical Conductivity of Nanosheaves of CeO_2. *Chem. Mater.* **2009**, *21*, 1182–1186.
59. He, J.; Han, M.; Shen, X.; Xu, Z. Crystal Hierarchically Splitting in Growth of $BaWO_4$ in Positive Cat−Anionic Microemulsion. *J. Cryst. Growth* **2008**, *310*, 4581–4586.
60. Chen, G.-Y.; Dneg, B.; Cai, G.-B.; Zhang, T.-K.; Dong, W.-F.; Zhang, W.-X.; Xu, A.-W. The Fractal Splitting Growth of Sb_2S_3 and Sb_2Se_3 Hierarchical Nanostructures. *J. Phys. Chem. C* **2008**, *112*, 672–679.
61. Ota, J.; Roy, P.; Srivastava, S. K.; Nayak, B. B.; Saxena, A. K. Morphology Evolution of Sb_2S_3 under Hydrothermal Conditions: Flowerlike Structure to Nanorods. *Cryst. Growth Des.* **2008**, *8*, 2019–2023.
62. Busch, S.; Dolhaine, H.; Dechesne, A.; Hinez, S.; Hochrein, O.; Laeri, F.; Podebrad, O.; Vietze, U.; Weiland, T.; Kniep, R. Biomimetic Morphogenesis of Fluorapatite−Gelatin Composites: Fractal Growth, the Question of Intrinsic Electric Fields, Core/Shell Assemblies, Hollow Spheres, and Reorganization of Denatured Collagen. *Eur. J. Inorg. Chem.* **1999**, *164*, 3–1653.
63. Colfen, H.; Qi, L. The Mechanism of the Morphogenesis of $CaCO_3$ in the Presence of Poly(ethylene glycol)-*B*-poly(methacrylic acid). *Prog. Colloid Polym. Sci.* **2001**, *117*, 200–203.
64. Wang, T.; Colfen, H.; Antonietti, M. Nonclassical Crystallization: Mesocrystals and Morphology Change of $CaCO_3$ Crystals in the Presence of a Polyelectrolyte Additive. *J. Am. Chem. Soc.* **2005**, *127*, 3246–3247.
65. Peters, F.; Epple, M. Crystallisation of Calcium Phosphates under Constant Conditions with a Double Diffusion Set-Up. *J. Chem. Soc., Dalton Trans.* **2001**, 3585–3592.
66. Park, R. J.; Meldrum, F. C. Shape-Constraint as a Route to Calcite Single Crystals with Complex Morphologies. *J. Mater. Chem.* **2004**, *14*, 2291–2296.
67. Park, R. J.; Meldrum, F. C. Synthesis of Single Crystals of Calcite with Complex Morphologies. *Adv. Mater.* **2004**, *14*, 1167–1169.
68. Dong, L.; Chu, Y.; Zhang, W. A Very Simple and Low Cost Route to Bi_2S_3 Nanorods Bundles and Dandelion-like Nanostructures. *Mater. Lett.* **2008**, *62*, 4269–4272.
69. Sharabani, R.; Reuveni, S.; Noy, G.; Shapira, E.; Sadeh, S.; Selzer, Y. Fabrication of Very High Aspect Ratio Metal Nanowires by a Self-Propulsion Mechanism. *Nano Lett.* **2008**, *8*, 1169–1173.
70. Brambilla, G.; Payne, D. N. The Ultimate Strength of Glass Silica Nanowires. *Nano Lett.* **2009**, *9*, 831–835.
71. Zhang, Z.; Shao, X.; Yu, H.; Wang, Y.; Han, M. Morphosynthesis and Ornamentation of 3D Dendritic Nanoarchitectures. *Chem. Mater.* **2005**, *17*, 332–336.
72. Imanaka, N.; Masui, T.; Itaya, M. Synthesis of an Environmentally Friendly and Nontoxic New Pigment Based on Rare Earth Phosphate. *Chem. Lett.* **2003**, *32*, 400–401.
73. Imanaka, N.; Masui, T.; Hirai, H.; Adachi, G. Y. Amorphous Cerium−Titanium Solid Solution Phosphate as a Novel Family of Band Gap Tunable Sunscreen Materials. *Chem. Mater.* **2003**, *15*, 2289–2291.
74. Yu, L.; Song, H.; Liu, Z.; Yang, L.; Lu, S.; Zheng, Z. Remarkable Improvement of Brightness for the Green Emissions in Ce^{3+} and Tb^{3+} Co-Activated $LaPO_4$ Nanowires. *Solid State Commun.* **2005**, *134*, 753–757.
75. Yu, L.; Song, H.; Liu, Z.; Yang, L.; Zheng, Z.; Lu, S. Electronic Transition and Energy Transfer Processes in $LaPO_4$−Ce^{3+}/Tb^{3+} Nanowires. *J. Phys. Chem. B* **2005**, *109*, 11450–11455.
76. Buchold, D. H. M.; Feldmann, C. Microemulsion Approach to Non-agglomerated and Crystalline Nanomaterials. *Adv. Funct. Mater.* **2008**, *18*, 1002–1011.
77. Riwotzki, K.; Meyssamy, H.; Schnablegger, H.; Kornowski, A.; Haase, M. Liquid-Phase Synthesis of Colloids and Redispersible Powders of Strongly Luminescing $LaPO_4$:Ce, Tb Nanocrystals. *Angew. Chem., Int. Ed.* **2001**, *40*, 573–576.
78. Rambabu, U.; Munirathnam, N. R.; Prakash, T. L.; Buddhudu, S. Emission Spectra of $LnPO_4$:Re^{3+} (Ln = La, Gd; Re = Eu, Tb, and Ce) Powder Phosphors. *Mater. Chem. Phys.* **2003**, *78*, 160–169.
79. Fu, Z.; Bu, W. High Efficiency Green-Luminescent $LaPO_4$:Ce, Tb Hierarchical Nanostructures: Synthesis, Characterization, and Luminescence Properties. *Solid State Sci.* **2008**, *10*, 1062–1067.
80. Kompe, K.; Borchert, H.; Storz, J.; Lobo, A.; Adam, S.; Moller, T.; Haase, M. Green-Emitting $CePO_4$:Tb/$LaPO_4$ Core-Shell Nanoparticles with 70% Photoluminescence Quantum Yield. *Angew. Chem., Int. Ed.* **2003**, *42*, 5513–5516.
81. Blasse, G.; Bril, A. Energy Transfer in Tb^{3+}-Activated Cerium(III) Compounds. *J. Chem. Phys.* **1969**, *51*, 3252–3254.
82. Bourcet, J.-C.; Fong, F. K. Quantum Efficiency of Diffusion Limited Energy Transfer in $La_{1-X-Y}Ce_xTb_yPO_4$. *J. Chem. Phys.* **1974**, *60*, 34–39.
83. Jose, M. T.; Lakshmanan, A. R. Ce^{3+} to Tb^{3+} Energy Transfer in Alkaline Earth (Ba, Sr, or Ca) Sulphate Phosphors. *Opt. Mater.* **2004**, *24*, 651–659.
84. Zhang, C.; Chen, J.; Zhou, Y.; Li, D. Ionic Liquid-Based "All-in-One" Synthesis and Photoluminescence Properties of Lanthanide Fluorides. *J. Phys. Chem. C* **2008**, *112*, 10083–10088.
85. Patra, C. R.; Bhattacharya, R.; Patra, S.; Basu, S.; Mukherjee, P.; Mukhopadhyay, D. Inorganic Phosphate Nanorods Are a Novel Fluorescent Label in Cell Biology. *J. Nanobiotechnol.* **2006**, *4*, 1–15.
86. Patra, C. R.; Bhattacharya, R.; Patra, S.; Basu, S.; Mukherjee, P.; Mukhopadhyay, D. Lanthanide Phosphate Nanorods as Inorganic Fluorescent Labels in Cell Biology Research. *Clin. Chem.* **2007**, *53*, 2029–2031.
87. Hu, H.; Yu, M.; Li, F.; Chen, Z.; Gao, X.; Xiong, L.; Huang, C. Facile Epoxidation Strategy for Producing Amphiphilic up-Converting Rare-Earth Nanophosphors as Biological Labels. *Chem. Mater.* **2008**, *20*, 7003–7009.
88. Chen, J.; Chen, S.; Zhao, X.; Kuznetsova, L.; Wong, S. S.; Ojima, I. Functionalized Single-Walled Carbon Nanotubes as Rationally Designed Vehicles for Tumor-Targeted Drug Delivery. *J. Am. Chem. Soc.* **2008**, *130*, 16778–16785.
89. Kostarelos, K.; Lacerda, L.; Pastorin, G.; Wu, W.; Wieckowski, S.; Luangsivilay, J.; Godefroy, S.; Pantarotto, D.; Briand, J.-P.; Muller, S.; *et al.* Cellular Uptake of Functionalized Carbon Nanotubes Is Independent of Functional Group and Cell Type. *Nat. Nanotechnol.* **2007**, *2*, 108–113.
90. Alkilany, A. M.; Nagaira, P. K.; Hexel, C. R.; Shaw, T. J.; Murphy, C. J.; Wyatt, M. D. Cellular Uptake and Cytotoxicity of Gold Nanorods: Molecular Origin of Cytotoxicity and Surface Effects. *Small* **2009**, *5*, 701–708.
91. Chithrani, B. D.; Ghazani, A. A.; Chan, W. C. W. Determining the Size and Shape Dependence of Gold Nanoparticle Uptake into Mammalian Cells. *Nano Lett.* **2006**, *6*, 662–668.
92. Silin, V.; Weetall, H.; Vanderah, D. J. SPR Studies of the Nonspecific Adsorption Kinetics of Human IgG and BSA on Gold Surfaces Modified by Self-Assembled Monolayers. *J. Colloid Interface Sci.* **1997**, *185*, 94–103.
93. Rezwan, K.; Meier, L. P.; Rezwan, M.; Voros, J.; Textor, M.; Gauckler, L. J. Bovine Serum Albumin Adsorption onto Colloidal Al_2O_3 Particles: A New Model Based on Zeta Potential and UV-Visible Measurements. *Langmuir* **2004**, *20*, 10055–10061.
94. Palmer, R. J.; Butenhoff, J. L.; Stevens, J. B. Cytotoxicity of the Rare Earth Metals Cerium, Lanthanum, and Neodymium *in Vitro*: Comparisons with Cadmium in a Pulmonary Macrophage Primary Culture System. *Environ. Res.* **1987**, *43*, 142–156.
95. Jiang, J.; Gu, H.; Shao, H.; Devlin, E.; Papaefthymiou, G. C.; Ying, J. Y. Bifunctional Fe_3O_4-Ag Heterodimer Nanoparticles for Two-Photon Fluorescence Imaging and Magnetic Manipulation. *Adv. Mater.* **2008**, *20*, 4403–4407.
96. Guo, S.-R.; Gong, J.-Y.; Jiang, P.; Wu, M.; Lu, Y.; Yu, S.-H. Biocompatible, Luminescent Silver@Phenol Formaldehyde Resin Core-Shell Nanospheres: Large-Scale Synthesis and Application for *in Vivo* Bioimaging. *Adv. Funct. Mater.* **2008**, *18*, 872–879.